


Studying Oral Tissue via Real-Time High-Resolution Terahertz Spectroscopic Imaging

Shengxin Yang,^{1,2,†} Liang Ding,^{3,†} Shuai Wang,³ Chen Du,¹ Longcheng Feng,¹ Hongsong Qiu,¹ Caihong Zhang^{1,2,*}, Jingbo Wu,^{1,2} Kebin Fan,^{1,2} Biaobing Jin,^{1,2} Jian Chen,^{1,2} and Peiheng Wu¹

¹Research Institute of Superconductor Electronics, Nanjing University, Nanjing, 210023 China

²Purple Mountain Laboratories, Nanjing 211111, China

³Central Laboratory of Stomatology, Nanjing Stomatological Hospital, Medical School of Nanjing University, Nanjing 210093, China

 (Received 3 May 2022; revised 23 September 2022; accepted 18 January 2023; published 10 March 2023)

Terahertz (THz) waves are extremely sensitive to water content and biological composition (proteins, genes, and metabolites), which are the key regulator of cancer development. Hence, the application of THz spectroscopy and imaging is promising in the field of biomedicine, especially in cancer diagnosis. Currently, the diagnosis of cancer patients (including tumor borders, tumor stage, etc.) mainly rely on optical microscope observation of pathological slices. The preparation of the slices is complicated and time consuming, and the microscopic field of view is small, which cannot effectively guide the precise removal of the tumor during the operation in time. To solve this problem, a label-free real-time high-resolution near-field THz spectroscopy imaging technique was developed. In this study, we successfully apply this technique to the oral tissue. Compared with conventional point-by-point scanning terahertz time-domain spectroscopy imaging, this technique can exhibit a real-time imaging rate (as high as 20 frames/s at 512×1024 pixels) and a field of view approximately 5 mm in diameter with a spatial resolution up to $\lambda/10$ at 1 THz in near-field condition. The experimental results show that the terahertz spectroscopic imaging in this paper can clearly detect and identify not only biological tissues with different components, but also normal and cancerous tissues, as well as tissues with the same composition but different slice directions. This work lays an experimental foundation for the application of THz spectroscopy imaging to rapid label-free intraoperative diagnosis, and it provides a basis for promoting the wide application of THz technology in the biomedical field.

DOI: [10.1103/PhysRevApplied.19.034033](https://doi.org/10.1103/PhysRevApplied.19.034033)

I. INTRODUCTION

Cancer is a worldwide health problem and the high cancer mortality rate is mainly due to the lack of early diagnosis [1]. The diagnosis and treatment of cancer is a major challenge that faces human society. The timeliness and accuracy of diagnosis affect the selection and success rate of surgical methods [2]. Although a variety of alternative diagnosis and treatment techniques are emerging, to date, the fundamental causes, diagnosis techniques, and treatment methods of cancer have not been fully understood [3]. Currently, most cancer treatment methods involve surgical procedures wherein tumor cells and tumor tissues are removed via surgery [4]. Therefore, it is essential to determine whether the tumor has been completely removed and to assess the margin during surgery. Histopathological

examination (HE) using pathological biopsy is an examination method with diagnostic significance for cancer. However, intraoperative pathological biopsy usually takes approximately 30 min. Longer operation times put patients at increased risk of anaesthesia-related adverse reactions and complications. Hence, there is an urgent need for an imaging method that is faster, more sensitive, effective, and convenient than histopathological examination.

As an electromagnetic wave with a frequency in the infrared–microwave range, terahertz (THz) radiation (with a frequency of 0.1–10 THz and wavelength of 30 μm –3 mm) possesses huge potential in the field of medical imaging [5]. Under the action of various carcinogenic factors, normal tissues and cells have significant changes in genes, proteins, and metabolites, and then develop into abnormal cancerous tissues and tumor cells. Amounting evidence has proven that these biomolecules show a specific response to THz radiation. Broadband absorption that increased with frequency was observed for lyophilized powder samples of calf thymus DNA, amino acids, bovine

*chzhang@nju.edu.cn

†S. Yang and L. Ding contributed equally to this work.

serum albumin (BSA), and collagen in the 0.06–4.0 THz frequency range [6,7], indicating that THz radiation can produce an effective response to dysregulation and changes in genes. Therefore, the significant changes of proteins and metabolites in the process of normal cell carcinoma becoming tumor cells may be beneficial to tissue imaging, which is beneficial for finding the tumor border and reducing the waiting time for surgical treatment and ultimately aids in improving patient prognosis.

In recent years, feasibility tests of THz imaging have been conducted in tumor tissues in animals [8,9] and human organs, including the skin [10–12], colon [13,14], breast [15–20], stomach [21], and liver [22]. These studies have indicated that THz imaging can effectively visualize cancerous areas without the marking process required for optical imaging. When compared with conventional medical imaging methods, terahertz imaging does not require labeling of samples and mainly recognizes component characteristics, showing the potential for faster, easier, and more accurate identification of malignant tumors and normal tissues [23,24]. However, the spatial resolution of traditional far-field terahertz spectroscopy imaging is lower than the diffraction limit, generally on the order of submillimeters to millimeters, and relies on point-by-point scanning of the sample, resulting in a very long imaging time [25,26]. Although THz-SNOM (scanning near-field optical microscopy) based on probe scanning technology [27] and THz s-SNOM based on atomic force microscopy technology [28] can achieve ultrahigh spatial resolution to the submicron or even nanometer level, conditions such as a measurement time that is too long, expensive to probe, and requiring the sample to be very flat make it unsuitable for imaging biological tissue samples. In addition, some terahertz imaging systems use single-frequency continuous-wave emission sources, which lack spectral information [29,30].

In this study, we first apply a real-time high-resolution terahertz spectroscopy imaging system to oral tissue measurement. This technique can exhibit a real-time imaging rate as high as 20 fps (1024×512 pixels), a field of view of approximately 5 mm in diameter, and a spatial resolution beyond the diffraction limit. The experimental results show that the terahertz spectroscopy imaging technology in this paper cannot only clearly detect and identify biological tissues with different components, but also detect and identify normal and tumor diseased tissues, as well as tissues with the same composition but different sectional directions. With dehydrated biological tissue, we reveal the source of contrast in the terahertz spectral range and the impact of the change in tissue morphology and composition on terahertz image. These results confirm that real-time high-resolution terahertz spectroscopy is most likely to be applied in the field of biomedicine, especially in tumor diagnosis and surgery with high application potential.

II. METHODOLOGY AND CHARACTERIZATION

A. Real-time terahertz near-field imaging setup

As shown in Fig. 1(a) the LiNbO₃ crystal (1.3 mol % MgO doping, Oxide Corporation, Japan) is excited by 800-nm center wavelength Ti:sapphire femtosecond laser (pulse width <100 fs, repetition frequency of 1 kHz, Coherent Inc., USA) via the tilted-pulse-front scheme [31] to generate a strong THz-field pulse. According to the angular-spectrum principle, the electromagnetic waves transmitted through a sample can be expressed as

$$U(x, y, z) = \int \int_{-\infty}^{+\infty} A_0(f_x, f_y, z_0) \exp\left[\frac{j2\pi z}{\lambda} \sqrt{1 - (\lambda f_x)^2 - (\lambda f_y)^2}\right] \exp[j2\pi(f_x x + f_y y)] df_x df_y, \quad (1)$$

where (f_x, f_y) is the spatial frequency at the input plane, λ is the wavelength of the incident optical waves. $A_0(f_x, f_y, z_0)$ is the two-dimensional Fourier transformation of the optical field at the input plane and $U(x, y, z)$ is the diffraction pattern at the observation plane. When spatial frequencies satisfy the condition $f_x^2 + f_y^2 > 1/\lambda^2$, evanescent waves with details' information (high-frequency information) of the sample will rapidly attenuate as the propagation distance increases [32]. To realize a high resolution of near-field imaging, the test sample is placed close to the electro-optic (EO) crystal to reduce the dissipation of THz evanescent waves before propagating to the crystal. While the sample tissue and crystal are separated by quartz and the distance between them met the conditions of quasi-near-field imaging [33]. Both cases are described in detail in the following part about spatial resolution characterization. The THz electric field induces the Pockels effect in the EO crystal to realize the conventional balanced EO sampling scheme for measuring the THz signals. After passing through the polarization beam splitter (PBS) and the beam splitter (BS), one stream of the probe beam carrying sample information is transmitted to the CMOS camera (2048×2048 pixels, OMRON SENTECH Co., Ltd, Japan) to realize THz imaging, while the other stream reaches a pair of photodetectors to realize THz time-domain pulse-signal measurement simultaneously. The GaP crystal ((110) crystal orientation and 300 μm thick) is used for free-space EO sampling [34] in our experiments.

We adjust the optical elements in the tilted-pump-pulse-front scheme to out the quasi-parallel THz beam. This can realize sample imaging with a relatively large field of view while maintaining a high SNR. This is usually impossible for commonly used probe-scanning microscopes based on conventional THz transmitters. Figure 1(b) shows the THz beam intensity measured via an uncooled microbolometer

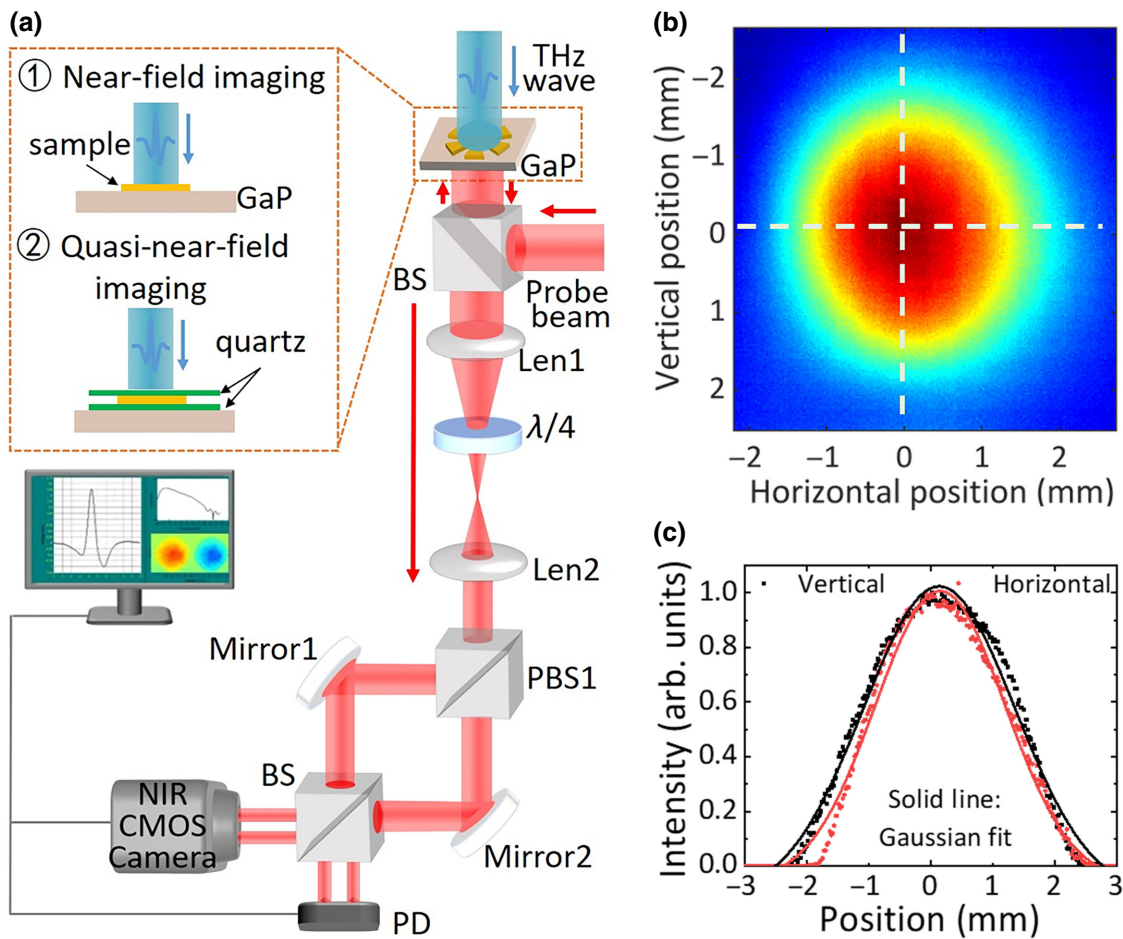


FIG. 1. Beam path diagram of THz spectroscopy microscope and characterization of THz beam. (a) Schematic diagram of the real-time EO near-field THz spectroscopy microscope; (b) THz beam intensity image captured via the THz camera; (c) cross-section intensity distribution along the white dashed line in the center of the beam in (b).

THz camera (320×240 pixels, IRV-T0831C, NEC Corporation, Japan) at 120 mm from the output surface of the LiNbO₃ crystal. The corresponding intensities along the horizontal and vertical axes through the THz beam center are shown in Fig. 1(c) (where the solid line denotes the Gaussian fit). From Fig. 1(c), we can obtain horizontal and vertical FWHM of 3.1 and 3.6 mm, respectively. By obtaining the cross-section intensity profile at several positions along the direction of propagation, the divergence of the THz beam is estimated based on a previous study [35]. The degree of divergence of the THz beam in the horizontal and vertical directions is 20 and 15.9 mrad, respectively. This satisfies the quasiparallelism required for high-quality imaging [36]. A calibrated pyroelectric photodetector (RM9-THz, Ophir Photonics, Israel) is used to evaluate the average power of the THz beam at the location of the EO crystal. At a relative humidity of up to 5%, the average power measured is approximately 1.55 mW and the electric field at the center of the THz beam is approximately 60 kV/cm.

Given that phase-locking technology is not applied in the CMOS camera, the SNR of the system is highly restricted. In addition to increasing the intensity of the THz radiation source, an effective method for improving the image SNR involves combining the dynamic subtraction technique [37] and pixel binning. By performing high-speed dynamic subtraction and pixel binning in a larger area during image acquisition, the SNR of the 2D THz image, obtained via a camera, becomes close to that of the signals measured using a single-point lock-in amplifier [38]. However, pixel binning for a larger area requires trade-offs in improving the sensitivity to a certain extent against the reduced resolution. In this study, all 4×4 pixels are combined into a new pixel to improve the SNR and sensitivity. Note that, the real-time imaging rate (as high as 20 frames/s at 512×1024 pixels) is the result of the combined effect of camera frame rate and dynamic subtraction technology. The frame rate of the camera is not fixed, it depends on the amount of data (i.e., the number of pixels used for imaging). While with dynamic subtraction

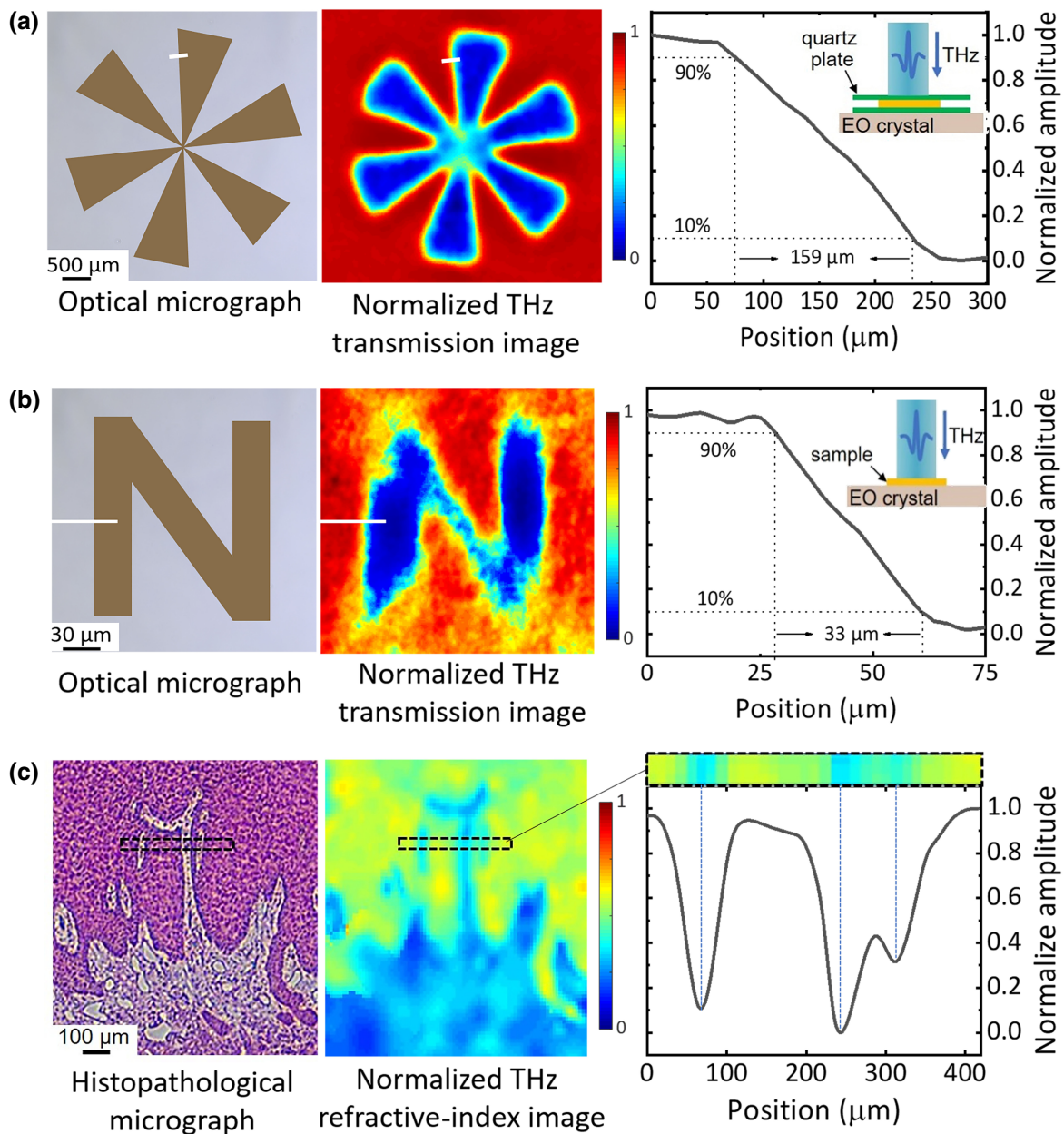


FIG. 2. Spatial-resolution characterization of the imaging system. (a) THz image of metal pinwheel at 1 THz under quasi-near-field conditions; (b) THz image of N-shaped letter at 1 THz under near-field conditions; (c) histopathological image of oral tissue and corresponding terahertz image under near-field conditions. The curve graph show the profiles extracted from the black dashed box in the terahertz image.

technique, the signal picture is obtained by the difference between even frames (signal and background) and odd frames (background) captured by the CMOS camera, which is synchronized to the modulation frequency.

B. Tissue sample preparation

An oral tissue sample was provided by the Nanjing University Medical College Affiliated Stomatological Hospital, and this study is approved by the Clinical Research

Ethics Committee of the institute. Tongue squamous cell carcinoma (TSCC) is the most common malignant tumor of the head and neck, originating from the tongue squamous epithelium cells. TSCC is highly malignant, prone to distant metastasis, and has a poor prognosis. Therefore, it is of great practical significance to select tongue squamous cell carcinoma and its adjacent tissues as test samples. After the sample was frozen, it was transferred to a cryostat (CM3050S, Leica Biosystems Nussloch GmbH, Germany) and embedded in the optimal cutting temperature (OCT)

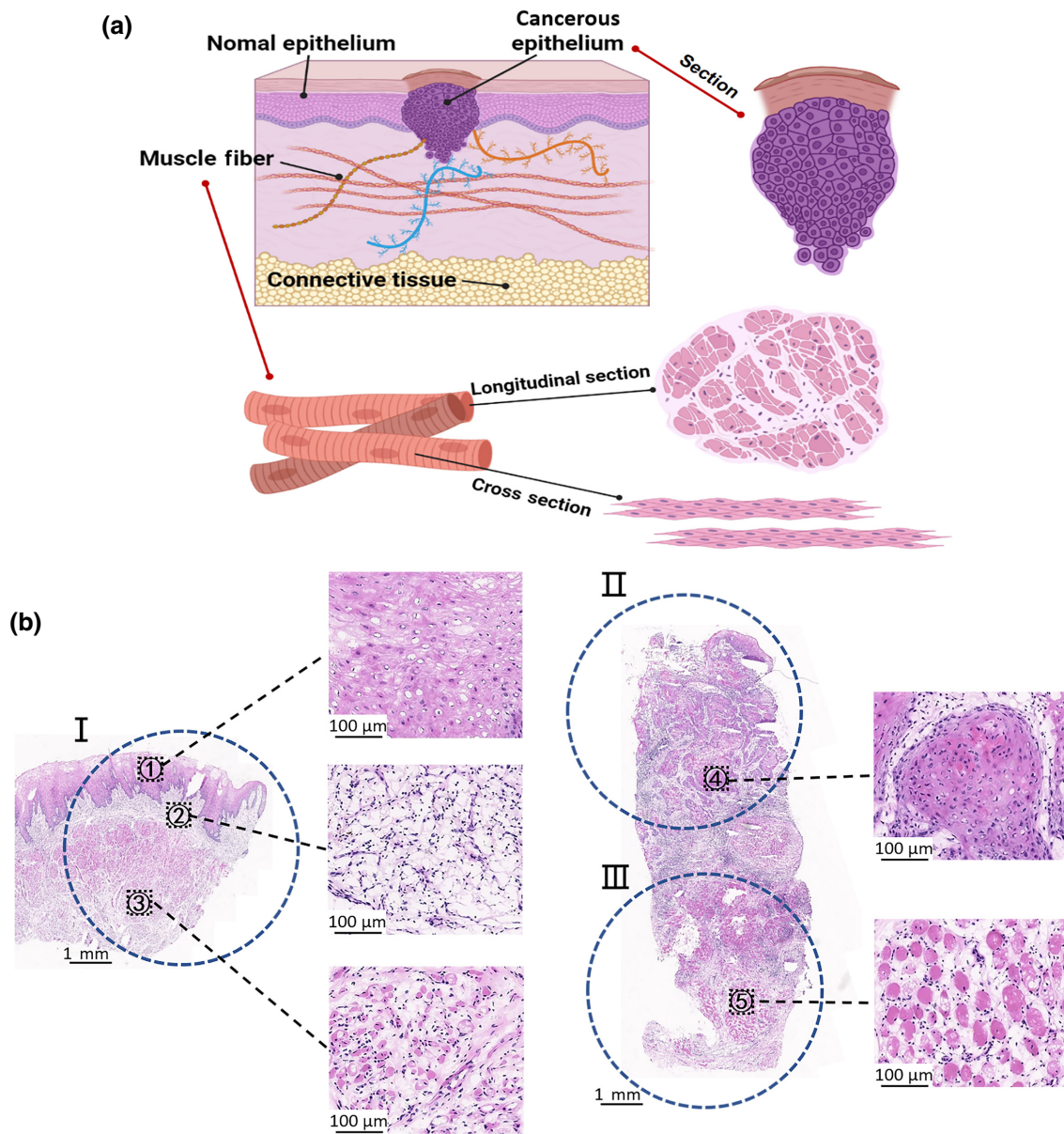


FIG. 3. Schematic diagram and histopathological image of the oral tissue. (a) Schematic diagram of the cross-section structure of the oral tissue, including normal epithelium, cancerous epithelium tissue, muscle fiber, connective tissue; (b) histopathological image of oral tissue. The tissue in the blue dotted circle is used for terahertz imaging: area I contains normal epithelial tissue ①, connective tissue ②, and muscle tissue (longitudinal section) ③; the tissue in area II is cancerous epithelium ④; the tissue in area III is muscle tissue (cross section) ⑤, and on the right are high-powered pathological images of areas.

compound (REF4583, Sakura Finetek USA Inc., USA) on a cryostat at a constant temperature of -20°C . Here, OCT compound is a water-soluble mixture of polyethylene glycol. At present, it has been widely used in immunohistochemical laboratory. Its purpose is to support tissue during frozen section, to increase tissue continuity, and reduce wrinkle and fragmentation. Then, the sample is cut into flat slices. A $5\text{-}\mu\text{m}$ -thick section of each tissue is placed on a glass slide, and histopathological evaluation is performed after H&E staining. A $100\text{-}\mu\text{m}$ -thick section of each tissue is packaged and used for THz-imaging

measurement. The prepared tissue sections are placed in a sample holder composed of two window plates (Quartz) to prevent tissue dehydration during sample transportation and maintain a flat sample surface during the experiment. The quartz window plates absorbed a minor portion of the wide-spectrum THz wave, and they are separated by a spacer of a certain thickness to match the thickness of the sample slice. In order to obtain the properties of the tissue sample in this work, modeling is set up to compare the theoretical propagation of the THz signal to the measured signal. The material parameter extraction

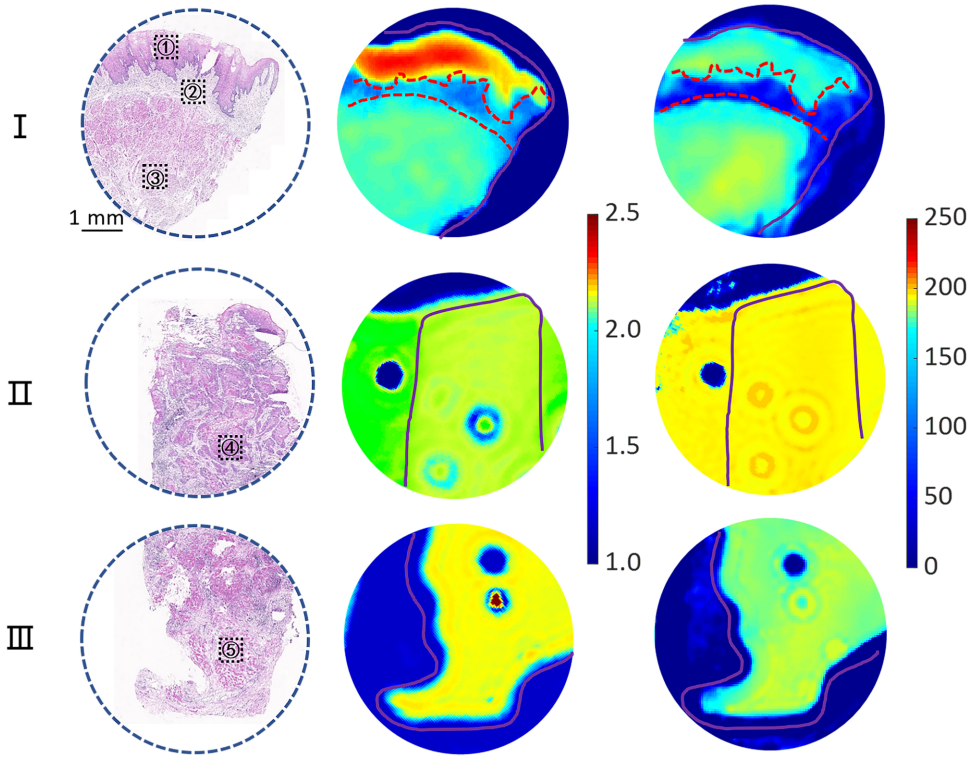


FIG. 4. Histopathological image and corresponding terahertz spectrum image: the left column are histopathological images, the middle column are the THz refractive-index images at 1 THz, and the right column are the THz absorption-coefficient images at 1 THz. The solid purple line is used to describe the outline of the tissue, and the red dashed line is used to assist in dividing the normal tissue of different components.

process requires these two spectra, $E_{\text{sam}}(\omega)$ and $E_{\text{ref}}(\omega)$, which are Fourier transformed from time-domain measurements about the holder with and without tissue sample. Normalizing the sample spectrum by the reference, yields the complex transfer function of the sample in the frequency domain:

$$T(\omega) = \frac{E_{\text{sam}}(\omega)}{E_{\text{ref}}(\omega)} = \tilde{\tau} e^{(\gamma_a - \gamma_t)d_t} = A e^{-j\Delta\varphi}, \quad (2)$$

where the ratio of transmission coefficients is expressed as $\tilde{\tau} = \tilde{n}_t(\tilde{n}_a + \tilde{n}_q)^2 / \tilde{n}_a(\tilde{n}_q + \tilde{n}_t)^2$, and $\gamma = j\tilde{n}\omega/c$ is the propagation constant. ω represents the angular frequency, c is the speed of light in vacuum, d_t is the thickness of sample tissue, and \tilde{n} is the complex refractive index of the dielectric medium (a , air; q , quartz; t , tissue). In the numerical solution, the theoretical values of magnitude (A) and phase ($\Delta\varphi$) are compared against the measurements obtained from the pulsed THz imaging system and minimize the error between them for obtaining the properties of the biological tissue [39].

C. Spatial resolution characterization

The analysis of the image resolution is shown in Fig. 2. The imaging spatial resolution of this system is

divided into the following two situations: quasi-near-field [Fig. 2(a)] and near-field [Fig. 2(b)]. We can evaluate the spatial resolution of the microscope by obtaining the spatial distance corresponding to the variation of the edge electric field amplitude from 10% to 90% in the image [27]. Figures 2(a) and 2(b) show the terahertz image of the metal mask and the intensity profile extracted at a specific location under quasi-near-field and near-field conditions. The linear spatial resolution is obtained from the electric field amplitude extracted along the white line in Figs. 2(a) and 2(b). The spatial resolution under quasi-near-field conditions is around $159 \mu\text{m}$ at 1 THz, which is close to $\lambda/2$, as shown in Fig. 2(a) using a $300\text{-}\mu\text{m}$ -thick GaP EO crystal detector. By using a thinner $20\text{-}\mu\text{m}$ -thick LiNbO₃ crystal to replace the $300\text{-}\mu\text{m}$ -thick GaP for reducing the diffraction of terahertz waves in the EO detection crystal, a higher spatial resolution can be achieved. Figure 2(b) shows N-shaped metal letter imaging with a line width of $30 \mu\text{m}$, achieving spatial resolution of $33 \mu\text{m}$ (approximately $\lambda/10$) at the frequency of 1 THz. We also imaged oral tissue samples as shown in Fig. 2(c). There is connective tissue texture, whose line width is about $37 \mu\text{m}$ (indicated by the black dotted box), distributed in epithelial tissue. Due to the use of a thinner EO crystal, the losses in sensitivity occur to some extent, and the uniformity and contrast of the

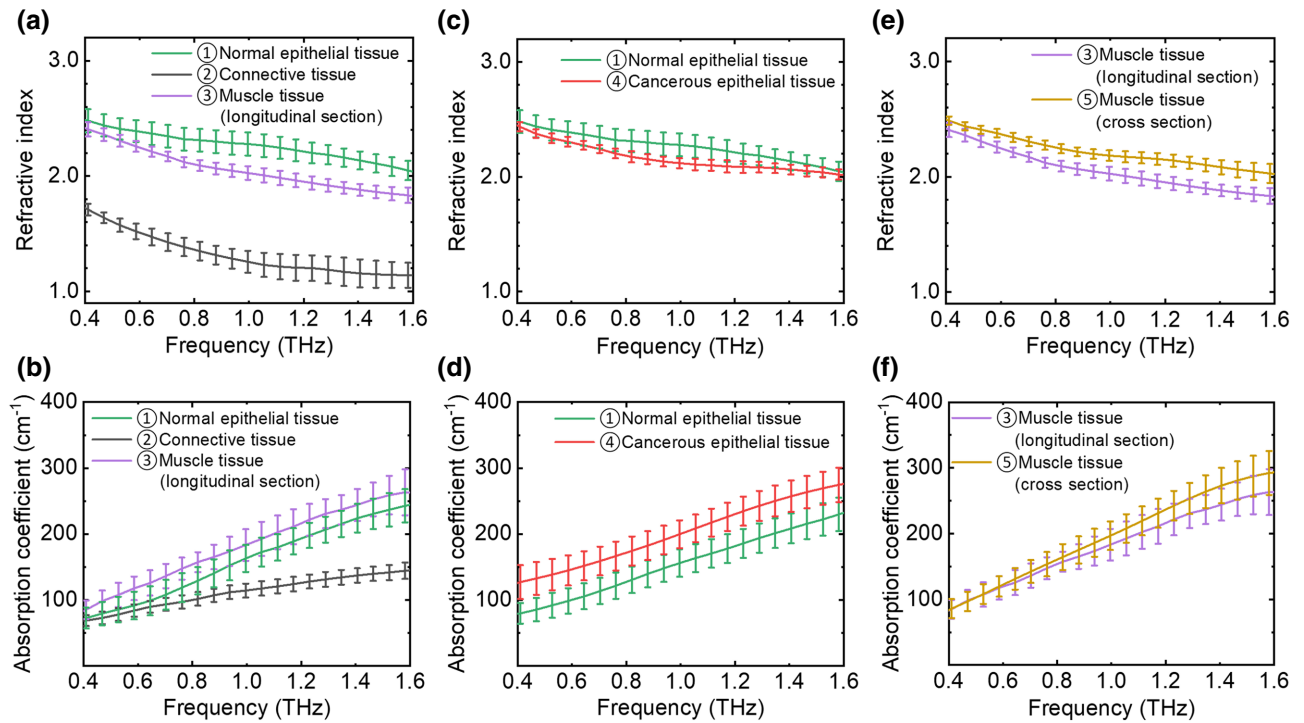


FIG. 5. Terahertz spectrum of oral tissue with different components. (a) Refractive-index spectrum and (b) absorption-coefficient spectrum of normal epithelial tissue, connective tissue, and muscle tissue (longitudinal section); (c) refractive-index spectrum and (d) absorption coefficient spectrum of epithelial tissue and tongue squamous cell carcinoma tissue; (e) refractive-index spectrum and (f) absorption coefficient spectrum of different sectional muscle tissues.

picture are relatively poor. The profiles extracted from the black dashed line demonstrate the clearly visible texture in the THz image, which means this imaging can distinguish biological target with $37\ \mu\text{m}$ size and shows the potential to discover tiny cancer lesions. The sandwich structure to retain the sample is not adopted to the condition for near-field imaging, and changes in water content during the sample-transfer process may be inevitable. Therefore, unless there are special circumstances, such as imaging of small cancer lesions, we usually conduct biological tissue imaging in a simple and easy way of quasi-near-field imaging in this paper.

III. RESULTS AND DISCUSSION

Figure 3(a) shows a schematic cross-section structure of the oral tissue, which contains the cell morphology and structural characteristics of normal and abnormal tissues. In order to obtain a representative spectral image, we select three representative areas for imaging according to the results of histopathological analysis, as shown by the blue dotted circle in the pathological picture in Fig. 3(b). The normal tissue in imaging area I contains three types of components: normal epithelial tissue ①, connective tissue ②, and muscle fiber ③. The tissue in imaging area II is tongue squamous cell carcinomas, which have the

characteristics of squamous cells. These cells are derived from normal epithelial cells that become cancerous. The tissue in imaging area III is tongue muscle tissue, which have rod-shaped or oval-shaped nuclei and eosinophilic cytoplasm in the cell.

In terahertz spectral-imaging experiments, it is often necessary to extract two key physical parameters, the refractive index and absorption coefficient, from the terahertz signal of the detected sample, to essentially determine the composition of the sample. We combine the spectral information extracted by each pixel into a two-dimensional image, and the spectral image of the sample is shown in Fig. 4. For imaging area I, the THz refractive index image clearly shows the regions in the sample for three different tissues. This is in good agreement with the corresponding H&E staining image. This is because the three types of tissues exhibit different refractive indices. As the refractive-index spectrum [Fig. 5(a)] shows, the refractive index of loose connective tissue is significantly lower than that of the other two tissues, while the refractive index of epithelial tissue is slightly higher than that of muscle fibers. Compared with the refractive-index image, the three types of tissues cannot be distinguished clearly in the absorption coefficient image, and only the loose connective tissue is vaguely distinguishable in the absorption coefficient image. Epithelial tissue and muscle fibers

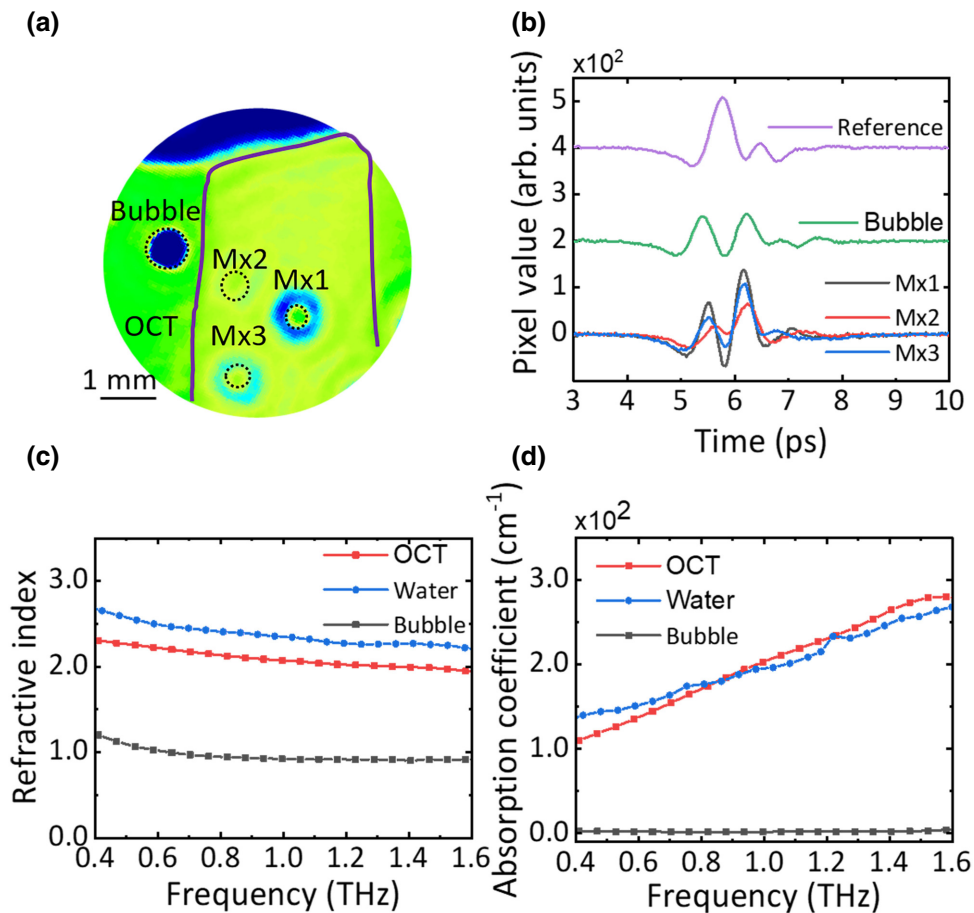


FIG. 6. Identification of substance within the specific area of THz image. (a) Refractive-index image of area II; (b) time-domain spectrum extracted from the specific area in (a); (c) refractive-index spectrum and (d) absorption coefficient of Bubble, OCT compound, and water.

(longitudinal slices) have similar absorption coefficients in the entire frequency spectrum [Fig. 5(b)], and loose connective tissues have absorption coefficients above 0.8 THz, which are different from the above-mentioned two tissues. In addition, the slight difference in the shape of the tissue area between the H&E image and the terahertz image is derived from the tiny structural changes between the pathological slice and the sample slice for imaging. In our study, 100-micron-thick slices used for terahertz imaging are much thicker than normal pathological slices. Compared with the thinner pathological slice, the sample slice tissue contains multiple layers of cells, and the cells have different distribution in each layer, resulting in differences between the terahertz image and the pathological slice. In addition, due to the diffraction effect of the tissue edge, the edge of the tissue presents a different spectral value compared with the internal area of the tissue in the terahertz image.

Imaging area II is cancerous epithelial tissue that is marked by the solid line in the terahertz spectrum image, which arises from abnormal lesions of epithelial tissue, we

extract the spectral information of these two tissues for comparison, as shown in Figs. 5(c) and 5(d). The average value of the THz refractive index of cancerous epithelial tissue is close to the average value of normal epithelial tissue, and their error bars mostly overlap. The absorption coefficient of cancerous epithelial tissue is significantly higher than that of normal epithelial tissue, which is related to the increase in water content caused by the presence of new blood vessels and tissue fluid in the cancer tissue [40]. We compare the absorption coefficient images of the tissues of the two regions at 1.0 THz. As shown in Fig. 4, the absorption coefficient images have obvious differences in color, but the refractive-index images are not obvious. Additionally, due to the embedded OCT compound, the OCT residue becomes attached to the sliced tissue during the sample-slicing process and denoted outside the brown line in Fig. 4(II). In the refractive-index image, the OCT compound showed a different refractive index from the cancerous epithelial tissue within the brown dashed line, but it was similar in the absorption coefficient image and could not be clearly distinguished.

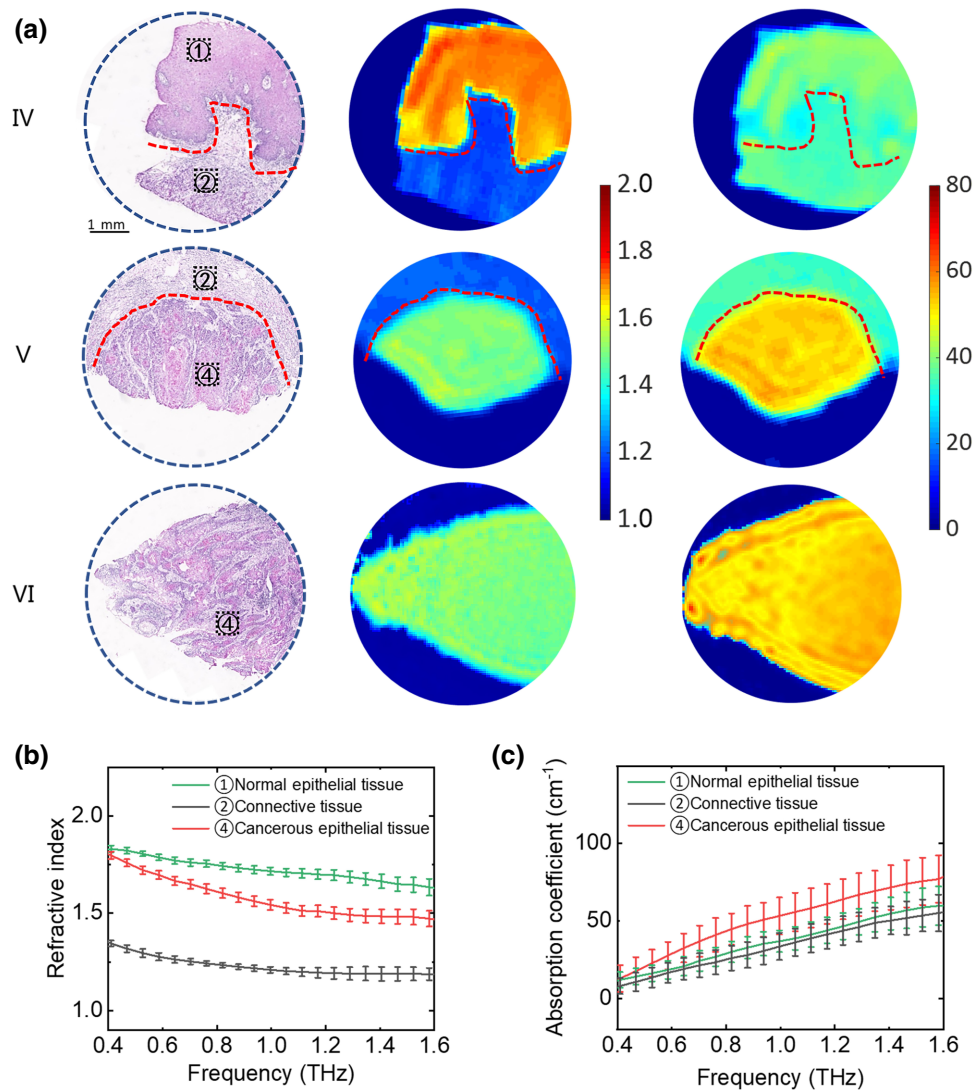


FIG. 7. Terahertz images and spectrum of lyophilized oral tissue. (a) Histopathological image and corresponding terahertz spectrum image [left, histopathological image; middle, THz refractive-index image (1.2 THz); right, THz absorption-coefficient image (1.2 THz)]; (b) refractive-index spectrum corresponding tissue; (c) absorption-coefficient spectrum corresponding tissue. The red dashed line is used to assist in dividing the oral tissue with different components.

Imaging area III is an image of muscle tissue (cross section). From the terahertz image, the refractive index of muscle tissue in area III is higher than that in area I. We extract the spectral information in the same way, as shown in Figs. 5(e) and 5(f). The two types of muscle tissues have significant differences in refractive index and similar absorption coefficients. By comparing the cell morphology of the two sections, we infer that the slice directions of the muscle tissues in two areas are different relative to the direction of the muscle fibers. The muscle tissue in area III is sliced transversely, and the muscle tissue in area I is sliced longitudinally. We infer that these two methods of slicing lead to differences in the density of muscle cells and therefore the difference in refractive index.

To maintain the activity of the sample, it is necessary to transfer the sample section to the imaging device under the freezing of dry ice. During the thawing process at room temperature, air bubbles will be generated inside and outside the sliced tissue area, as shown by the black dotted circle in Fig. 6(a). By comparing the time-domain signal of the marked area with the reference signal [Fig. 6(b)], there is a reflection signal in the marked area, which overlaps with the main pulse signal. In these marked areas, the dark blue area (Bubble) indicates that there are only simple bubbles in this area, and its spectral information is shown in Fig. 6(c), which is basically consistent with air. In addition, the other area (Mix) should be two layers of media containing tissue and bubbles at the same time. The extrusion of bubbles causes uneven media distribution. The refractive

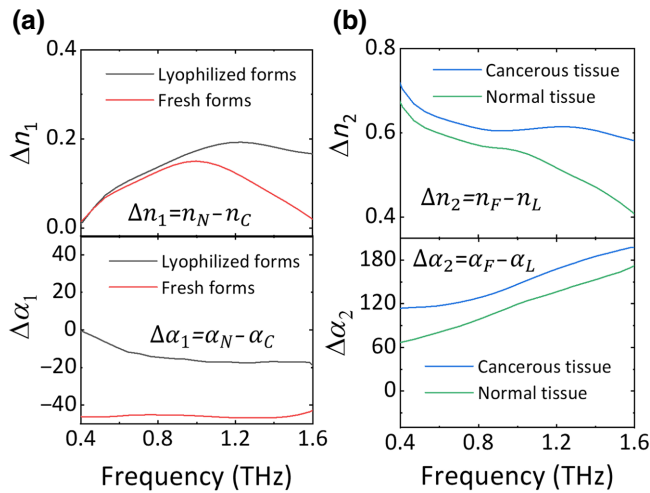


FIG. 8. (a) The difference between the normal and cancerous epithelial tissue in fresh and lyophilized forms: the difference of refractive index $\Delta n_1 = n_N - n_C$ and the difference of absorption coefficient $\Delta \alpha_1 = \alpha_N - \alpha_C$, where the subscripts N and C present normal and cancerous epithelial tissue; (b) the difference between fresh and lyophilized epithelial tissue: the difference of refractive index $\Delta n_2 = n_F - n_L$, and the difference of absorption coefficient $\Delta \alpha_2 = \alpha_F - \alpha_L$, where the subscripts F and L present fresh and lyophilized epithelial tissue.

index, which is sensitive to the thickness of the medium, presents different values at the center and the edge of the marking area, so the color of the refractive-index image is not uniform. At the same time, we extract the spectrum of the OCT solution outside the cancerous epithelial tissue and compared it with water [41] in the literature, as shown in Fig. 6(d). The OCT compound is a water-soluble mixture of polyethylene glycol and polyvinyl alcohol. This substance has an absorption coefficient like that of water. However, due to the presence of polyethylene glycol and polyvinyl alcohol, the refractive index is different from that of water. In the refractive-index image, the OCT compound shows a different refractive index from the cancerous epithelial tissue within the purple solid line, but it is similar in the absorption-coefficient image and cannot be clearly distinguished.

Lyophilization can remove large amounts of water and retain sample freshness, allowing for consistent and stable THz measurements [42]. Figure 7 presents terahertz images and spectrums of normal and cancerous epithelial tissue samples in lyophilized forms. Compared to fresh tissue, lyophilized tissue has a lower refractive index and absorption coefficient after dehydration. The difference between normal and cancerous epithelial tissue samples in the refractive index means contrast in the terahertz image mainly arises from tissue morphology and composition. It can be seen from the pathologically stained images that cancerous epithelial tissue has the characteristics of squamous cells where a small number of keratinizing beads

and intercellular bridges formed. Tumor cells have obvious atypia, and mitoses can be seen. There are varying degrees of lymphocyte infiltration and fibrosis in the tumor stroma. After dehydration, there is little difference between normal and cancerous epithelial tissue in the absorption coefficient, which demonstrates that water is the main source of the contrast difference in the terahertz absorption coefficient image. In addition, the terahertz spectrums of connective tissue do not change much after dehydration because of their low water content. Fresh tissues directly excised from specimens enabled the comprehensive assessment of both water content, morphology, and composition variations, while lyophilized tissues assessed the latter two [24]. This means that THz spectral images can distinguish normal and cancerous epithelial tissue in both fresh tissues and lyophilized tissues.

Few studies have reported that THz medical diagnostic imaging can be achieved using the physical properties of cells or tissues except for water content. To analyze the source of discrepancies in terahertz spectral images, we made a difference in the spectrum (shown in Fig. 8) between the normal and cancerous epithelial tissue in fresh and lyophilized forms, respectively. We define the difference in refractive index $\Delta n_1 = n_N - n_C$ and the difference in absorption coefficient $\Delta \alpha_1 = \alpha_N - \alpha_C$ between normal and cancerous epithelial tissue, where the subscripts N and C represent normal and cancerous epithelial tissue, respectively. We also define the difference in refractive index $\Delta n_2 = n_F - n_L$ and the difference of absorption coefficient $\Delta \alpha_2 = \alpha_F - \alpha_L$ between fresh and lyophilized epithelial tissue, where the subscripts F and L represent fresh and lyophilized epithelial tissue. As illustrated in Fig. 8(a), the refractive-index difference between the normal and cancerous epithelial tissue in lyophilized forms is greater than that in fresh forms, and so we can deduce that the contrast in the terahertz refractive-index image mainly arises from tissue morphology and composition, especially in the high-frequency band. Due to the high moisture content, cancer tissue with a low refractive index closed the gap with normal tissue in fresh form. This point can be verified in Fig. 8(b), where the blue line is higher than the green line, which means that water in the cancerous epithelial tissue increases the refractive index much more than that in normal tissue. From the absorption-coefficient difference in Fig. 8(a), we can also conclude that the absorption-coefficient difference between the normal and cancerous epithelial tissue in fresh forms is larger than twofold of that in lyophilized forms. Similarly, water content plays an important role in the absorption-coefficient contrast between normal and cancerous epithelial tissue in its fresh form. As illustrated in Fig. 8(b), the absorption-coefficient difference between the cancerous epithelial fresh and lyophilized tissue is higher than that between normal epithelial fresh and lyophilized tissue. Excluding the influence of morphology and composition factors, this

relationship is more accurate to indicate that cancerous epithelial tissue is richer in water than normal epithelial tissue.

To determine the structural changes that occurred in cancerous epithelial tissue, we examine the histopathology results. From the pathologically stained images, cancerous epithelial tissue has the characteristics of squamous cells where a small number of keratinizing beads and intercellular bridges formed. Tumor cells demonstrate evidence of obvious atypia and mitoses. There are varying degrees of lymphocyte infiltration and fibrosis in the tumor stroma. Compared to dense normal epithelial tissue, cancerous epithelial tissue thus exhibits different responses to terahertz signals at the cellular level.

IV. CONCLUSION

In this study, the feasibility of real-time high-resolution THz near-field spectroscopy imaging for the intraoperative diagnosis of unlabeled cancer tissue is examined. The experimental results indicate that the proposed THz imaging technique exhibits faster imaging speed than probe scanning THz microscopy (essential for intraoperative diagnosis), higher resolution than conventional THz time-domain spectroscopy imaging, and more spectral properties than CW THz imaging. Furthermore, it is equipped with label-free, high-speed, and high-resolution large field of view, and it exhibits high performance with spectral information, which can be applied in THz biomedical detection fields. In future studies, the technique will be improved further by reducing the thickness of the slice tissue, improving the imaging quality, and applying it to various biological detection applications.

ACKNOWLEDGMENTS

We thank financial support from the National Key Research and Development Program of China (2017YFA0700202, 2021YFB2800701), National Natural Science Foundation of China (NSFC) (62222106, 61871212, 62071217, 62027807, 92163216, 62288101), the Fundamental Research Funds for the Central Universities, and Natural Science Foundation of Jiangsu Province (BK20190300).

-
- [1] Y. Pu, L. Ding, Y. Wang, Y. Wang, S. Chen, X. Huang, Z. He, Y. Ni, and Q. Hu, Biopsy pattern of invasion type to determine the surgical approach in early-stage oral squamous cell carcinoma, *Virchows Arch.* **479**, 109 (2021).
- [2] Y. Mirahmadi, R. Nabavi, F. Taheri, M. M. Samadian, Z. N. Ghale-Noie, M. Farjami, A. Samadi-Khouzani, M. Yousefi, S. Azhdari, A. Salmaninejad, and A. Sahebkar, MicroRNAs as biomarkers for early diagnosis, prognosis, and therapeutic targeting of ovarian cancer, *J. Oncol.* **2021**, 3408937 (2021).

- [3] J. Qu, F. S. Kalyani, L. Liu, T. Cheng, and L. Chen, Tumor organoids: synergistic applications, current challenges, and future prospects in cancer therapy, *Cancer Commun.* **41**, 1331 (2021).
- [4] J. M. Jung, J. Y. Cho, W. J. Lee, S. E. Chang, M. W. Lee, and C. H. Won, Emerging minimally invasive technologies for the detection of skin cancer, *J. Pers. Med.* **11**, 951 (2021).
- [5] B. Ferguson and X.-C. Zhang, Materials for terahertz science and technology, *Nat. Mater.* **1**, 26 (2002).
- [6] L. Xie, Y. Yao, and Y. Ying, The application of terahertz spectroscopy to protein detection: A review, *Appl. Spectrosc. Rev.* **49**, 448 (2014).
- [7] Y. Ueno, R. Rungsawang, I. Tomita, and K. Ajito, Quantitative measurements of amino acids by terahertz time-domain transmission spectroscopy, *Anal. Chem.* **78**, 5424 (2006).
- [8] S. Yamaguchi, Y. Fukushi, O. Kubota, T. Itsuji, T. Ouchi, and S. Yamamoto, Brain tumor imaging of rat fresh tissue using terahertz spectroscopy, *Sci. Rep.* **6**, 30124 (2016).
- [9] S. J. Oh, S.-H. Kim, Y. B. Ji, K. Jeong, Y. Park, J. Yang, D. W. Park, S. K. Noh, S.-G. Kang, Y.-M. Huh, *et al.*, Study of freshly excised brain tissues using terahertz imaging, *Biomed. Opt. Express* **5**, 2837 (2014).
- [10] V. P. Wallace, A. J. Fitzgerald, S. Shankar, N. Flanagan, R. Pye, J. Cluff, and D. D. Arnone, Terahertz pulsed imaging of basal cell carcinoma ex vivo and in vivo, *Br. J. Dermatol.* **151**, 424 (2004).
- [11] K. I. Zaytsev, K. G. Kudrin, V. E. Karasik, I. V. Reshetov, and S. O. Yurchenko, In vivo terahertz spectroscopy of pigmented skin nevi: Pilot study of non-invasive early diagnosis of dysplasia, *Appl. Phys. Lett.* **106**, 053702 (2015).
- [12] D. Li, Z. Yang, A. Fu, T. Chen, L. Chen, M. Tang, H. Zhang, N. Mu, S. Wang, G. Liang, and H. Wang, Detecting melanoma with a terahertz spectroscopy imaging technique, *Spectrochim. Acta A Mol. Biomol. Spectrosc.* **234**, 118229 (2020).
- [13] F. Wahaia, I. Kasalynas, R. Venckevicius, D. Seliuta, G. Valusis, A. Urbanowicz, G. Molis, F. Carneiro, C. D. Carvalho Silva, and P. L. Granja, Terahertz absorption and reflection imaging of carcinoma-affected colon tissues embedded in paraffin, *J. Mol. Struct.* **1107**, 214 (2016).
- [14] H. Chen, S. Ma, X. Wu, W. Yang, and T. Zhao, Diagnose human colonic tissues by terahertz near-field imaging, *J. Biomed. Opt.* **20**, 036017 (2015).
- [15] Q. Cassar, A. Al-Ibadi, L. Mavarani, P. Hillger, J. Grzyb, G. MacGrogan, T. Zimmer, U. R. Pfeiffer, J. P. Guillet, and P. Mounaix, Pilot study of freshly excised breast tissue response in the 300–600 GHz range, *Biomed. Opt. Express* **9**, 2930 (2018).
- [16] T. C. Bowman, M. El-Shenawee, and L. K. Campbell, Terahertz imaging of excised breast tumor tissue on paraffin sections, *IEEE Trans. Antennas Propag.* **63**, 2088 (2015).
- [17] B. S. Peter, S. Yngvesson, P. Siqueira, P. Kelly, A. Khan, S. Glick, and A. Karellas, Development and testing of a single frequency terahertz imaging system for breast cancer detection, *IEEE J. Biomed. Health Inform.* **17**, 785 (2013).
- [18] H. Chen, W.-J. Lee, H.-Y. Huang, C.-M. Chiu, Y.-F. Tsai, T.-F. Tseng, J.-T. Lu, W.-L. Lai, and C.-K. Sun, Performance of THz fiber-scanning near-field microscopy to diagnose breast tumors, *Opt. Express* **19**, 19523 (2011).

- [19] P. C. Ashworth, E. Pickwell-MacPherson, E. Provenzano, S. E. Pinder, A. D. Purushotham, M. Pepper, and V. P. Wallace, Terahertz pulsed spectroscopy of freshly excised human breast cancer, *Opt. Express* **17**, 12444 (2009).
- [20] A. J. Fitzgerald, V. P. Wallace, M. Jimenez-Linan, L. Bobrow, R. J. Pye, A. D. Purushotham, and D. D. Arnone, Terahertz pulsed imaging of human breast tumors, *Radiology* **239**, 533 (2006).
- [21] Y. Bin Ji, C. H. Park, H. Kim, S.-H. Kim, G. M. Lee, S. K. Noh, T.-I. Jeon, J.-H. Son, Y.-M. Huh, S. Haam, *et al.*, Feasibility of terahertz reflectometry for discrimination of human early gastric cancers, *Biomed. Opt. Express* **6**, 1398 (2015).
- [22] L. Rong, T. Latychevskaia, C. Chen, D. Wang, Z. Yu, X. Zhou, Z. Li, H. Huang, Y. Wang, and Z. Zhou, Terahertz in-line digital holography of human hepatocellular carcinoma tissue, *Sci. Rep.* **5**, 8445 (2015).
- [23] Z. Yan, L.-G. Zhu, K. Meng, W. Huang, and Q. Shi, THz medical imaging: from in vitro to in vivo, *Trends Biotechnol.* **40**, 816 (2022).
- [24] X. Yang, X. Zhao, K. Yang, Y. Liu, Y. Liu, W. Fu, and Y. Luo, Biomedical applications of terahertz spectroscopy and imaging, *Trends Biotechnol.* **34**, 810 (2016).
- [25] B. B. Hu and M. C. Nuss, Imaging with terahertz waves, *Opt. Lett.* **20**, 1716 (1995).
- [26] D. M. Mittleman, R. H. Jacobsen, and M. C. Nuss, T-ray imaging, *IEEE J. Sel. Top. Quantum Electron.* **2**, 679 (1996).
- [27] H.-T. Chen, R. Kersting, and G. C. Cho, Terahertz imaging with nanometer resolution, *Appl. Phys. Lett.* **83**, 3009 (2003).
- [28] T. L. Cocker, V. Jelic, R. Hillenbrand, and F. A. Hegmann, Nanoscale terahertz scanning probe microscopy, *Nat. Photonics* **15**, 558 (2021).
- [29] T. Löffler, K. J. Siebert, N. Hasegawa, T. Hahn, and H. G. Roskos, All-optoelectronic terahertz imaging systems and examples of their application, *Proc. IEEE* **95**, 1576 (2007).
- [30] K. J. Siebert, H. Quast, R. Leonhardt, T. Löffler, M. Thomson, T. Bauer, H. G. Roskos, and S. Czasch, Continuous-wave all-optoelectronic terahertz imaging, *Appl. Phys. Lett.* **80**, 3003 (2002).
- [31] J. A. Fülöp, L. Pálfalvi, G. Almási, and J. Hebling, Design of high-energy terahertz sources based on optical rectification, *Opt. Express* **18**, 12311 (2010).
- [32] L. Mandel and E. Wolf, *Optical Coherence and Quantum Optics* (Cambridge University Press, Cambridge, 1995).
- [33] X. Wang, Y. Cui, D. Hu, W. Sun, J. Ye, and Y. Zhang, Terahertz quasi-near-field real-time imaging, *Opt. Commun.* **282**, 4683 (2009).
- [34] Q. Wu and X. C. Zhang, Free-space electro-optic sampling of terahertz beams, *Appl. Phys. Lett.* **67**, 3523 (1995).
- [35] M. Kunitski, M. Richter, M. D. Thomson, A. Vredenburg, J. Wu, T. Jahnke, M. Schöffler, H. Schmidt-Böcking, H. G. Roskos, and R. Dörner, Optimization of single-cycle terahertz generation in LiNbO₃ for sub-50 femtosecond pump pulses, *Opt. Express* **21**, 6826 (2013).
- [36] H. Hirori, A. Doi, F. Blanchard, and K. Tanaka, Single-cycle terahertz pulses with amplitudes exceeding 1 MV/cm generated by optical rectification in LiNbO₃, *Appl. Phys. Lett.* **98**, 091106 (2011).
- [37] X. Wang, Y. Cui, W. Sun, J. Ye, and Y. Zhang, Terahertz real-time imaging with balanced electro-optic detection, *Opt. Commun.* **283**, 4626 (2010).
- [38] Z. Jiang, X. G. Xu, and X. C. Zhang, Improvement of terahertz imaging with a dynamic subtraction technique, *Appl. Opt.* **39**, 2982 (2000).
- [39] T. Bowman, M. El-Shenawee, and L. K. Campbell, Terahertz transmission vs reflection imaging and model-based characterization for excised breast carcinomas, *Biomed. Opt. Express* **7**, 3756 (2016).
- [40] L. Yu, L. Hao, T. Meiqiong, H. Jiaoqi, L. Wei, D. Jinying, C. Xueping, F. Weiling, and Z. Yang, The medical application of terahertz technology in non-invasive detection of cells and tissues: opportunities and challenges, *RSC Adv.* **9**, 9354 (2019).
- [41] E. Pickwell, B. E. Cole, A. J. Fitzgerald, V. P. Wallace, and M. Pepper, Simulation of terahertz pulse propagation in biological systems, *Appl. Phys. Lett.* **84**, 2190 (2004).
- [42] G. M. Png, J. W. Choi, B. W.-H. Ng, S. P. Micken, D. Abbott, and X.-C. Zhang, The impact of hydration changes in fresh bio-tissue on THz spectroscopic measurements, *Phys. Med. Biol.* **53**, 3501 (2008).